Prestack wave-equation depth migration in elliptic coordinates

Jeff Shragge* **and Guojian Shan***

**Stanford Exploration Project,*

Geophysics Department,

Stanford University,

Stanford, CA 94305

(March 17, 2008)

GEO-2007-0231

Running head: **Elliptic Coordinate PSDM**

ABSTRACT

We extend Riemannian wavefield extrapolation (RWE) to prestack migration using 2D elliptic coordinate systems. The corresponding 2D elliptic extrapolation wavenumber introduces only an isotropic slowness model stretch to the single-square-root operator. This enables the use of existing Cartesian finite-difference extrapolators for propagating wavefields on elliptic meshes. A post-stack migration example illustrates the advantages of elliptic coordinates for imaging turning waves. A 2D imaging test using a velocity benchmark data set demonstrates that the RWE prestack migration algorithm generates high-quality prestack migration images that are more accurate than those generated by Cartesian operators of the equivalent accuracy. We note that even in situations where RWE geometries are employed, a high-order implementation of the one-way extrapolator operator is required for accurate

propagation and imaging. We discuss potential extensions of the analytical approach to 3D RWE coordinate systems.

INTRODUCTION

Wave-equation migration techniques based on one-way extrapolators are often used for accurate imaging of complex geologic structures. Most conventional downward continuation approaches, though, are unable to handle the steeply propagating or turning wave components often important for imaging areas of interest. A number of novel imaging approaches address these issues through a judicious decomposition of recorded wavefields [e.g., plane-wave migration (Whitmore, 1995)], partial and complete propagation-domain decomposition [e.g., Gaussian beam (Hill, 2001) and Riemannian wavefield extrapolation (Sava and Fomel, 2005; Shragge, 2006), respectively], or a combination thereof [e.g. plane-wave migration in tilted coordinates (Shan and Biondi, 2004)]. These techniques have overcome many, though not all, issues in the practical application of one-way extrapolation operators.

Riemannian wavefield extrapolation (RWE) is a method for propagating wavefields on generalized coordinate meshes. The central idea of RWE is to transform the computational domain from Cartesian to a geometry where the extrapolation axis is oriented along the general wavefield propagation direction. Ideally, solving the corresponding one-way extrapolation equations in the transform domain leads to the bulk of wavefield energy being propagated at angles relatively near to the extrapolation axis, thus improving the global accuracy of wavefield extrapolation. One obvious application is generating high-quality Green's functions for point-sources in a dynamic coordinate system, where a suite of rays is first traced through a velocity model and then used as the skeleton on which to propagate wavefields.

Although the full-domain decomposition approach naturally adapts to propagation in a point-source ray-coordinate system, two unresolved issues make it difficult to apply RWE

efficiently in prestack shot-profile migration algorithms. First, receiver wavefields in shot-profile migration are usually broadband in plane-wave dip spectrum and cannot be easily represented by a single coordinate system (i.e., reflections from opposing dips propagate in opposing directions). Second, the optimal meshes for the source and receiver wavefields usually do not share a common geometry. For example, a polar coordinate system is well suited for propagating source wavefields, while elliptic meshes are more appropriate for receiver wavefields. This factor is detrimental to algorithmic efficiency where images are generated by correlating source and receiver wavefields: by existing on different grids they must both be interpolated to a common Cartesian reference frame prior to imaging. This leads to a significant number of interpolations, which leaves the algorithm computationally unattractive, except in target-oriented imaging situations.

The main goal of this paper is to specify a single coordinate system that enables the accurate propagation of high-angle and turning wave components of both the source and receiver wavefields. We demonstrate that an elliptic coordinate system forms a natural computational grid for prestack shot-profile migration and has useful geometric properties that facilitate numerical implementation. An elliptic coordinate system originates on the horizontal acquisition surface and steps outward as a series of ellipses. Thus, the coordinate system expands in a radial-like manner appropriate for computing accurate point-source Green's functions while allowing the dipping plane-wave components in the receiver wavefield to propagate at large angles to either side of the acquisition surface. One consequence of using a 2D elliptic coordinate system is that the corresponding extrapolation operator must be modified; however, we show that elliptic geometry introduces only an isotropic velocity model stretch. Existing high-order implicit Cartesian finite-difference extrapolators with accuracy up to 80° from the extrapolation axis (Lee and Suh, 1985) can be used to

propagate wavefields, readily enabling accurate imaging of wide-angle and turning waves at a cost competitive with that of Cartesian downward continuation.

This paper begins with a discussion of why elliptic meshes are a natural coordinate system choice for shot-profile prestack depth migration (PSDM). We develop an extrapolation wavenumber appropriate for wavefield propagation on a 2D elliptic coordinate system. We then present post-stack and prestack migration examples that illustrate the scheme's ability to image steep structure using turning waves. The paper concludes with a discussion on the advantages of analytic coordinate systems relative to more dynamically generated meshes, and two potential extensions of the analytical approach to 3D RWE coordinate systems.

ELLIPTIC COORDINATE EXTRAPOLATION

Generating an effective RWE coordinate system for prestack migration requires appropriately linking mesh geometry with wavefield propagation kinematics. Figure 1a illustrates this concept for an idealized shot-profile imaging experiment through a medium of constant wavefield slowness s. Here, we specify source and receiver wavefields ($\mathcal{S}$ and $\mathcal{R}$) as impulses at source position and time $[\mathbf{x_s}, \tau_s = 0]$ and at receiver position and time $[\mathbf{x_r}, \tau_r = \tau]$, where τ is an arbitrary time lag. The wavefields expand outward as spherical wavefronts (dashed lines) according to

$$\mathcal{S}(\mathbf{x_s}, \mathbf{x}; t) = \delta\left(t - s\,||\mathbf{x} - \mathbf{x_s}||\right) \quad \text{and} \quad \mathcal{R}(\mathbf{x_r}, \mathbf{x}; t) = \delta\left(t - \tau + s\,||\mathbf{x} - \mathbf{x_r}||\right), \tag{1}$$

where $||\mathbf{x}||$ is the Euclidean norm of the vector $\mathbf{x}$ and s is wavefield slowness. An image $\mathcal{I}(\mathbf{x})$ can be generated by applying a correlation imaging condition at $t = 0$ (Claerbout, 1985),

$$\mathcal{I}(\mathbf{x}) = \delta\left(\tau - s(||\mathbf{x} - \mathbf{x_r}|| + ||\mathbf{x} - \mathbf{x_s}||)\right), \tag{2}$$

which is the equation of an ellipse (solid line).

This suggests a natural correspondence between an elliptic coordinate system and the prestack migration isochrons for a constant velocity model. One can observe this in Figure 1 by how well the isochron image conforms to the underlying coordinate mesh. In this example, we intentionally did not fix the locations of the elliptic mesh foci relative to $\mathbf{x_s}$ and $\mathbf{x_r}$. Adjusting these points will alter both the elliptic mesh and how well it conforms to the isochrons. These parameters represents two degrees of freedom that allow us to match mesh geometry to the bulk propagation direction.

The Helmholtz equation in Elliptic coordinates

Propagating a wavefield Ψ in generalized coordinates requires encoding the mesh geometry directly into the one-way extrapolation equations (Sava and Fomel, 2005; Shragge, 2006). Hence, deriving an elliptic-coordinate extrapolation operator requires introducing elliptic geometry into the Laplacian operator ∇^2 of the Helmholtz equation,

$$\nabla^2\Psi + \omega^2 s^2 \Psi = 0. \tag{3}$$

We begin with the definition of the analytic transformation between the elliptic and Cartesian coordinate systems (Morse and Feshbach, 1953),

$$\begin{bmatrix} x_1 \\ \\ x_2 \end{bmatrix} = \begin{bmatrix} a\cosh\xi_2\cos\xi_1 \\ \\ a\sinh\xi_2\sin\xi_1 \end{bmatrix}, \tag{4}$$

where $[x_1, x_2]$ are the underlying Cartesian coordinate variables, $[\xi_1, \xi_2]$ are the RWE elliptic coordinates defined on the intervals $\xi_1 \in [0, \pi)$, and $\xi_2 \in [0, \infty]$, and a is a stretch parameter controlling coordinate system breadth. (Note that the definition in equation 4 is analogous to the definitions of cylindrical or spherical coordinates.) As illustrated in Figure 1, lines

of constant ξ_3 represent ellipses, while those of constant ξ_1 form hyperbolas. Figure 1 also shows our definition of the angle, $\theta(\xi)$, between the elliptic and Cartesian coordinates systems. Additional information on elliptic coordinates is presented in Appendix A.

The metric tensor ($g_{ij} = \frac{\partial x_k}{\partial \xi_i}\frac{\partial x_k}{\partial \xi_j}$ with an implicit sum over index k) describing the elliptic coordinate system geometry is

$$[g_{ij}] = \begin{bmatrix} A^2 & 0 \\ 0 & A^2 \end{bmatrix}, \tag{5}$$

where $A = a\sqrt{\sinh^2 \xi_2 + \sin^2 \xi_1}$. The metric tensor determinant, $|\mathbf{g}| = A^4$, is required to specify the associated (g^{ij}, or the inverse of g_{ij}) and weighted ($m^{ij} = \sqrt{|\mathbf{g}|}\, g^{ij}$) metric tensors,

$$\left[g^{ij}\right] = \begin{bmatrix} A^{-2} & 0 \\ 0 & A^{-2} \end{bmatrix} \quad \text{and} \quad \left[m^{ij}\right] = \begin{bmatrix} 1 & 0 \\ 0 & 1 \end{bmatrix}. \tag{6}$$

Interestingly, the weighted metric tensor m^{ij} in equations 6 is an identity matrix, indicating that the transformation in equation 4 causes space to contract or dilate isotropically.

Inserting the tensor components in equations 6 into the standard expression for the Laplacian operator (Morse and Feshbach, 1953),

$$\nabla^2 = \frac{1}{\sqrt{|\mathbf{g}|}}\frac{\partial}{\partial \xi_i}\left(\sqrt{|\mathbf{g}|}g^{ij}\frac{\partial}{\partial \xi_j}\right) = \frac{1}{\sqrt{|\mathbf{g}|}}\frac{\partial}{\partial \xi_i}\left(m^{ij}\frac{\partial}{\partial \xi_j}\right), \tag{7}$$

leads to the elliptic coordinate Laplacian operator,

$$\nabla^2 = \frac{1}{A^2}\left(\frac{\partial^2}{\partial \xi_2^2} + \frac{\partial^2}{\partial \xi_1^2}\right). \tag{8}$$

The elliptic coordinate Helmholtz equation is derived by introducing equation 8 into equation 3 and rearranging terms to yield

$$\left[\frac{\partial^2}{\partial \xi_2^2} + \frac{\partial^2}{\partial \xi_1^2}\right]\Psi + A^2\omega^2 s^2 \Psi = 0. \tag{9}$$

Defining an "effective slowness" field $s_{eff} = As$, we may rewrite the above as

$$\left[\frac{\partial^2}{\partial \xi_2^2} + \frac{\partial^2}{\partial \xi_1^2}\right] \Psi + \omega^2 s_{eff}^2 \Psi = 0. \tag{10}$$

Equation 10 is this paper's most important result: an elliptic coordinate system introduces only an isotropic slowness model stretch in the Helmholtz equation.

Dispersion relation in Elliptic coordinates

Deriving an elliptic-coordinate dispersion relation from equation 10 proceeds in the usual manner. In the following 2D development, we use the convention that ξ_2 and ξ_1 are the extrapolation direction and orthogonal coordinate, respectively. Replacing the partial differential operators with their Fourier domain duals (Claerbout, 1985), gives

$$k_{\xi_1}^2 + k_{\xi_2}^2 = \omega^2 \, s_{eff}^2, \tag{11}$$

and isolating the k_{ξ_2} wavenumber contributions leads to a recursive wavefield extrapolation operator for stepping outward in concentric ellipses in the ξ_2 direction,

$$\Psi(\xi_2 + \Delta\xi_2, k_{\xi_1}, \omega) = \Psi(\xi_2, k_{\xi_1}, \omega) \mathrm{e}^{\pm \mathrm{i} \Delta\xi_2 k_{\xi_2}} = \Psi(\xi_2, k_{\xi_1}, \omega) \mathrm{e}^{\pm \mathrm{i} \Delta\xi_2 \sqrt{\omega^2 s_{eff}^2 - k_{\xi_1}^2}}, \tag{12}$$

where $\Delta\xi_2$ is the extrapolation step size, and $\pm$ determines whether a wavefield is propagating causally (i.e., source wavefield) or acausally (i.e., receiver wavefield).

The dispersion relation in equation 12 will not be an exact expression in general because s_{eff} varies spatially. This situation is similar to that in Cartesian wavefield extrapolation in laterally varying media, and equation 12 can be easily implemented with existing Cartesian extrapolation schemes (e.g., finite differences, PSPI) and using an effective slowness model $s_{eff} = As$.

An additional question worth addressing is to which angle is propagation in elliptic coordinates accurate? Because the geometric effects of the elliptic coordinate can be incorporated into an effective slowness model, s_{eff}, the local angular accuracy for finite-difference propagation is equivalent to that of a Cartesian-domain implementation. Globally, though, the maximum propagation angle, for a given extrapolation accuracy, depends on the orientation of the local extrapolation axis. Figure 1b illustrates how the angle of the extrapolation axis, $\theta = \theta(\boldsymbol{\xi})$, locally changes in an elliptic coordinate system. In the following examples, our $\pm 80^\circ$ finite-difference propagators (Lee and Suh, 1985) will have a maximum extrapolation angle equal to $\theta(\boldsymbol{\xi}) \pm 80^\circ$.

Prestack migration algorithm

The expression in equation 12 can be extended to prestack migration. An initial step is defining the foci locations of the elliptic coordinate system. Unfortunately, choosing the optimal answer, relative to the acquisition geometry (i.e., the source and farthest-offset locations), is not straightforward. For example, situating foci too close together pulls the wavefields towards the focus because the local extrapolation axis angle, θ, rapidly becomes steep (c.f., Figure 1b). In contrast, placing foci too distant from each other leads to a near-rectilinear coordinate system that affords little improvement over Cartesian extrapolation. We determined heuristically that optimal foci locations are an additional $10 - 20\%$ (of the aperture length) beyond the source point and farthest receiver offset.

The remaining prestack migration algorithmic steps are:

1. Specify a shot-specific elliptic coordinate system for source location s_i, and interpolate the Cartesian velocity model to this mesh;

2. generate the shot-specific image, $\mathcal{I}(\boldsymbol{\xi}, s_i)$, in the elliptic coordinate system at step ξ_2 from the source, $\mathcal{S}$, and receiver, $\mathcal{R}$, wavefields

$$\mathcal{I}(\boldsymbol{\xi}, s_i) = \sum_{\omega} \Re \left[\mathcal{S}^*(\boldsymbol{\xi}, \omega, s_i) \mathcal{R}(\boldsymbol{\xi}, \omega, s_i) \right]; \tag{13}$$

3. propagate source and receiver wavefields (for all frequencies) by a step $\Delta\xi_2$

$$\begin{aligned} \mathcal{S}(\xi_2 + \Delta\xi_2, k_{\xi_1}, \omega, s_i) &= \mathcal{S}(\xi_2, k_{\xi_1}, \omega, s_i)\, \mathrm{e}^{+\mathrm{i}\Delta\xi_2 k_{\xi_2}}, \\ \mathcal{R}(\xi_2 + \Delta\xi_2, k_{\xi_1}, \omega, s_i) &= \mathcal{R}(\xi_2, k_{\xi_1}, \omega, s_i)\, \mathrm{e}^{-\mathrm{i}\Delta\xi_2 k_{\xi_2}}; \end{aligned} \tag{14}$$

4. repeat steps 2-3 until reaching the end of the elliptic coordinate mesh;

5. interpolate the single-shot, elliptic-coordinate image $\mathcal{I}(\boldsymbol{\xi}, s_i)$ to Cartesian coordinates and update the global Cartesian image $\mathcal{I}(\boldsymbol{x})$; and

6. repeat steps 1-5 for all shot locations.

2D MIGRATION TESTS

This section presents 2D test results for a post-stack turning-wave and the prestack velocity benchmark (Billette and Brandsberg-Dahl, 2005) data sets. We propagate all wavefields with the one-way extrapolators described in Lee and Suh (1985) on an elliptic coordinate system defined by equation 4 assuming effective slowness fields $s_{eff} = As$. Imaging results are generated using post-stack and shot-profile migration algorithms employing the recursive extrapolation relations in equations 12 and 14, respectively. Image volumes in elliptic coordinates are subsequently transformed back to the Cartesian domain using sinc interpolation. The extra computational cost of generating the RWE migration results, relative to those in Cartesian imaging, is roughly two additional interpolations per shot: one for

the Cartesian velocity model to the elliptic mesh, and another for the elliptic image to the Cartesian grid.

Post-stack migration example

The first elliptic coordinate migration example uses the post-stack data set shown in Figure 2. The data were generated from an adapted Sigsbee model, shown in Figure 3a, using exploding reflector (two-way time-domain FD) modeling from all salt body edges (Sava, 2006). The imaging test involved only the turning components of the wavefield shown in Figure 2. Figure 3a also presents the experimental geometry for the coordinate system with foci situated at -90 km (not shown) and 5 km. Because the propagation directions of the wavefield are known, we were able to chose foci locations that ensured that the grid generally conformed to the turning wave propagation direction. (We recognize that this example is a special case where the dip field is oriented largely in one direction.) Figure 3b shows the effective slowness model, s_{eff}, in the transformed coordinate system parameterized by extrapolation step and surface take-off position axes.

Figure 4 presents the results for migration in the chosen RWE elliptic coordinates. Panel 4a shows the monochromatic post-stack migration result with the elliptic coordinate system overlain. Post-stack migration in elliptic coordinates successfully propagates turning waves, which arrive at normal incidence to the salt flank, as expected for exploding-reflector modeling. Panel 4b shows the elliptic-coordinate version of the image in Panel 4a at successive extrapolation steps, and illustrates that wavefield energy propagates at angles fairly steep relative to the extrapolation axis. Panels 4c and 4d show the broadband image results in Cartesian and elliptic coordinate systems, respectively. The salt flanks beneath the salt

nose are accurately positioned, demonstrating the potential for imaging turning waves in elliptic coordinates with wide-angle extrapolation operators.

Prestack migration example

We performed a prestack elliptic coordinate migration test using a velocity benchmark model (Figure 5a). Full data offsets were not used for each shot; rather, we used a 10-km initial migration aperture to enable more accurate propagation of turning waves within our propagation domain. The foci for each migrated shot were located at an additional 15% (of the 10-km acquisition aperture) beyond the shot point and the farthest receiver offset. Panel 5b shows the effective slowness model, s_{eff}, in the elliptic coordinate system. The elliptic mesh is parameterized by extrapolation step and surface take-off position axes. Importantly, the steep salt body structure to the right becomes relatively low angle under this coordinate transformation, and should be better imaged.

Figure 6 presents the prestack migration results for the elliptic coordinate system. Panel 6a shows the RWE shot-profile migration result in elliptic coordinates, while panel 6b presents the corresponding Cartesian image generated by finite-difference operators of equivalent accuracy. (Note that slightly different source wavelets were used in the two migrations leading to a phase rotation between the two images.) The salt body to the left is well-imaged in most areas in both images, though is improved in, for example, the circled location. The salt body flanks to the right (circled locations), illuminated largely by turning and prismatic waves are better imaged in the elliptic system.

Discussion

One question naturally arising when using RWE propagation in a prestack migration algorithm is how does one obtain the optimal trade-off between using i) low-order extrapolators on a more dynamic coordinate system (e.g., ray coordinates); and ii) high-order extrapolators on a mesh less conformal to the wavefield propagation direction. Based on our experience, we argue that a parametric coordinate system (such as a tilted Cartesian or an elliptic mesh) offers the advantage of developing analytic extrapolation operators that readily lend themselves to high-order finite-difference schemes. While coordinate systems based on ray-tracing better conform to the wavefield propagation direction, numerically generated meshes do not lend themselves as easily to high-order extrapolators because of the greater number, and spatially variability, of the corresponding mixed-domain coefficients. In addition, analytic coordinates allow the user to specify a coordinate system adequate for propagating both the source and receiver wavefields, rather than optimizing for one or the other. One caveat, however, is that higher-order extrapolators are usually required for analytic coordinate systems because, though they are more optimal for global propagation, they are less conformal to the local extrapolation direction.

A second question worth addressing is how can the analytic coordinate approach be extended to 3D prestack shot-profile migration? Although a complete study of 3D possibilities is beyond the scope of the paper, two candidate coordinate systems for wavefield extrapolation in the ξ_3 direction are elliptic cylindrical and oblate spheroidal coordinates. (These coordinate systems are discussed in Appendix B).

The elliptic cylindrical coordinate system, shown in Figure 7, extends the 2D elliptic mesh invariantly in the second lateral dimension (ξ_2 now) and leads to a fairly basic ex-

pression for the extrapolation wavenumber k_{ξ_3} (see Appendix B). This coordinate system should be well suited for narrow-azimuth geometries where the elliptic surfaces (i.e., ξ_1) are oriented in the inline direction, leaving the cylindrical coordinate (i.e., ξ_2) to extend in the crossline direction. One disadvantage is that waves cannot be overturned in the crossline direction; the degree to which this is problematic, though, largely depends on the velocity model and reflector geometry.

The oblate spheroidal coordinates, shown in Figure 8, incorporates a more spherical-like geometry and would enable steep-angle and turning wave propagation at all azimuths. This coordinate system likely is well suited for wide-azimuth data sets containing arrivals from a rich swath of azimuths. One drawback, though, is that this geometry leads to a more complicated and difficult-to-implement expression for extrapolation wavenumber k_{ξ_3} (see Appendix B).

Overall, the applicability of imaging in 3D analytic coordinate systems remains an open research topic that will be addressed by the authors in a future paper.

CONCLUSIONS

This paper extends Riemannian wavefield extrapolation to 2D prestack shot-profile migration. We choose an elliptic coordinate system that generally conforms to the wave propagation direction and enables wide-angle extrapolation of both source and receiver wavefields. Post-stack migration results of a turning wave data set validate the approach, while the 2D prestack imaging results show that the RWE migration algorithm generates images more accurate than the corresponding Cartesian results. The cost difference between the elliptic and Cartesian imaging algorithms is only two additional interpolations per migrated shot

profile. Finally, we argue that parametric coordinate systems are a good trade-off between the competing constraints of meshes conformal to the wavefield propagation direction and coordinate system simplicity because one can readily develop analytic wavenumbers and more accurate high-order extrapolation implementations.

ACKNOWLEDGMENTS

We thank Biondo Biondi, Ben Witten, Brad Artman, and Ken Larner for enlightening discussions. We thank the SEP sponsors for their continuing support, and we acknowledge BP for the synthetic velocity data set.

REFERENCES

Billette, F. and S. Brandsberg-Dahl, 2005, The 2004 BP velocity benchmark: 67th meeting, Expanded Abstracts, B035, Eur. Assn. Geosci. Eng.

Claerbout, J., 1985, Imaging the Earth's Interior: Stanford University.

Hill, N. R., 2001, Prestack Gaussian-beam depth migration: Geophysics, **66**, 1240–1250.

Lee, M. W. and S. Y. Suh, 1985, Optimization of one-way wave-equations (short note): Geophysics, **50**, 1634–1637.

Morse, P. and H. Feshbach, 1953, Methods of theoretical physics: Cambridge University Press.

Sava, P., 2006, Imaging overturning reflections by Riemannian Wavefield Extrapolation: Journal of Seismic Exploration, **15**, 209–223.

Sava, P. C. and S. Fomel, 2005, Riemannian wavefield extrapolation: Geophysics, **70**, T45–T56.

Shan, G. and B. Biondi, 2004, Imaging overturned waves by plane-wave migration in tilted coordinates: 74th Ann. Internat. Mtg., Expanded Abstracts, 969–972, Soc. of Expl. Geophys.

Shragge, J., 2006, Non-orthogonal Riemannian wavefield extrapolation, *in* Expanded Abstracts, 2236–2240, 75^{th} SEG Ann. Gen. Meeting and Exhibition.

Whitmore, N. D., 1995, An imaging hierarchy for common angle plane wave seismograms, *in* Ph.D. thesis, University of Tulsa.

APPENDIX A

ELLIPTIC COORDINATE SYSTEMS

Similar to cylindrical or spherical coordinate systems, the relationships between Cartesian and elliptic geometris in equation 4 cannot be derived *per se*. Exploring constant coordinate surfaces, however, provides additional insight into some characteristics of the elliptic coordinate system. As illustrated by the following trigonometric identities, curves of constant ξ_1 represent hyperbolas

$$\frac{x_1^2}{a^2\cos^2\xi_1} - \frac{x_2^2}{a^2\sin\xi_1} = \cosh^2\xi_2 - \sinh^2\xi_2 = 1, \tag{A-1}$$

while curves of constant ξ_2 form ellipses

$$\frac{x_1^2}{a^2\cosh^2\xi_2} + \frac{x_2^2}{a^2\sinh\xi_2} = \cos^2\xi_2 + \sin^2\xi_2 = 1. \tag{A-2}$$

Thus, outward extrapolation in the ξ_2 direction would step a wavefield through a family of elliptic surfaces defined by equation A-2.

Equation A-1 may also be used to derive an expression that defines the local extrapolation axis angle, $\theta(\boldsymbol{\xi})$, relative to vertical reference. Taking the total derivative of equation A-1,

$$\frac{2\,x_1\,\mathrm{d}x_1}{a^2\cosh^2\xi_1} + \frac{2\,x_2\,\mathrm{d}x_2}{a^2\sinh^2\xi_1} = 0, \tag{A-3}$$

and further manipulating the result yields the local extrapolation axis angle $\theta(\boldsymbol{\xi})$

$$\tan\theta = \frac{\mathrm{d}x_1}{\mathrm{d}x_2} = \frac{x_2\cos^2\xi_1}{x_1\sin^2\xi_1} = \tanh\xi_2\cot\xi_1. \tag{A-4}$$

Figure 1a illustrates these angles for the elliptic coordinate system.

APPENDIX B

ONE-WAY EXTRAPOLATION IN 3D COORDINATE SYSTEMS

This appendix develops the dispersion relationship for extrapolating waves for two 3D elliptic coordinate systems: elliptic cylindrical and oblate spheroidal. Readers interested in a more complete theoretical development are directed to Shragge (2006).

Elliptic Cylindrical Coordinates

The analytic transformation between the elliptic cylindrical and Cartesian coordinate systems is

$$\begin{bmatrix} x_1 \\ x_2 \\ x_3 \end{bmatrix} = \begin{bmatrix} a\cosh\xi_3\cos\xi_1 \\ \xi_2 \\ a\sinh\xi_3\sin\xi_1 \end{bmatrix}, \tag{B-1}$$

where $[x_1, x_2, x_3]$ are the underlying Cartesian coordinate variables, $[\xi_1, \xi_2, \xi_3]$ the RWE elliptic cylindrical coordinates defined on intervals $\xi_1 \in [0, 2\pi), \xi_2 \in [-\infty, \infty]$ and $\xi_3 \in [0, \infty]$, and parameter a is a stretch parameter controlling the breadth of the coordinate system.

The metric tensor ($g_{ij} = \frac{\partial x_k}{\partial \xi_i}\frac{\partial x_k}{\partial \xi_j}$) describing the geometry of the elliptic coordinate system is given by,

$$[g_{ij}] = \begin{bmatrix} A^2 & 0 & 0 \\ 0 & 1 & 0 \\ 0 & 0 & A^2 \end{bmatrix}, \tag{B-2}$$

where $A = a\sqrt{\sinh^2\xi_3 + \sin^2\xi_1}$. The determinant of the metric tensor is: $|\mathbf{g}| = A^4$. The

associated (inverse) metric tensor is given by,

$$\left[g^{ij}\right] = \begin{bmatrix} A^{-2} & 0 & 0 \\ 0 & 1 & 0 \\ 0 & 0 & A^{-2} \end{bmatrix}, \tag{B-3}$$

and weighted metric tensor ($m^{ij} = \sqrt{|\mathbf{g}|}\, g^{ij}$) is given by,

$$\left[m^{ij}\right] = \begin{bmatrix} 1 & 0 & 0 \\ 0 & A^2 & 0 \\ 0 & 0 & 1 \end{bmatrix}. \tag{B-4}$$

The corresponding extrapolation wavenumber is generated by using tensors g^{ij} and m^{ij} in the general wavenumber expression for 3D non-orthogonal coordinate system (Shragge, 2006). Note that even though the elliptic coordinate system varies spatially, the local curvature parameters ($n^i = \frac{\partial m^{ij}}{\partial \xi^j}$) remain constant: $n^1 = n^2 = n^3 = 0$. Thus, inserting the values of g^{ij}, m^{ij} and n^j leads to the following extrapolation wavenumber, k_{ξ_3}, for stepping outward in concentric ellipses,

$$k_{\xi_3} = \pm\sqrt{A^2 s^2 \omega^2 - k_{\xi_1}^2 - A k_{\xi_2}^2}. \tag{B-5}$$

The wavenumber for 2D extrapolation in elliptic coordinates reduces to

$$k_{\xi_3}|_{k_{\xi_2}=0} = \pm\sqrt{A^2 s^2 \omega^2 - k_{\xi_1}^2}. \tag{B-6}$$

Oblate Spheroidal Coordinates

The analytic transformation between the oblate spheroidal and Cartesian coordinate systems is

$$\begin{bmatrix} x_1 \\ x_2 \\ x_3 \end{bmatrix} = \begin{bmatrix} a\cosh\xi_3\cos\xi_1\cos\xi_2 \\ a\cosh\xi_3\cos\xi_1\sin\xi_2 \\ a\sinh\xi_3\sin\xi_1 \end{bmatrix}. \tag{B-7}$$

where coordinates are defined on intervals $\xi_1 \in [0, 2\pi), \xi_2 \in [0, 2\pi)$ and $\xi_3 \in [0, \infty]$, a is a stretch parameter controlling the breadth of the coordinate system. The metric tensor g_{ij} describing the geometry of oblate spheroidal coordinates is,

$$[g_{ij}] = \begin{bmatrix} A^2 & 0 & 0 \\ 0 & B^2 & 0 \\ 0 & 0 & A^2 \end{bmatrix}, \tag{B-8}$$

where $A = a\sqrt{\sinh^2\xi_3 + \sin^2\xi_1}$ and $B = a\cosh\xi_3\cos\xi_1$. The metric tensor determinant is given by $|\mathbf{g}| = A^4\,B^2$, the associated (inverse) metric tensor by,

$$\left[g^{ij}\right] = \begin{bmatrix} A^{-2} & 0 & 0 \\ 0 & B^{-2} & 0 \\ 0 & 0 & A^{-2} \end{bmatrix}, \tag{B-9}$$

and the weighted metric tensor by,

$$\left[m^{ij}\right] = \begin{bmatrix} B & 0 & 0 \\ 0 & \frac{A^2}{B} & 0 \\ 0 & 0 & B \end{bmatrix}. \tag{B-10}$$

We generate the corresponding extrapolation wavenumber by inputting tensors g^{ij} and m^{ij} into the generalized wavenumber expression for 3D non-orthogonal coordinate systems (Shragge, 2006). Unlike in elliptic cylindrical coordinates, though, the oblate spheroidal

system has non-stationary n^i coefficients: $n^1 = a\cosh\xi_3\sin\xi_1$, $n^2 = 0$ and $n^3 = a\sinh\xi_3$. The resulting extrapolation wavenumber is

$$k_{\xi_3} = \frac{\mathrm{i}\tanh\xi_3}{2} \pm \sqrt{A^2 s^2\omega^2 - k_{\xi_1}^2 - \frac{\sqrt{\sinh^2\xi_3 + \sin^2\xi_1}}{\cosh\xi_3\cos\xi_1}k_{\xi_2}^2 + \mathrm{i}k_{\xi_1}\tan\xi_1 - \frac{1}{4}\tanh^2\xi_3}. \quad \text{(B-11)}$$

The wavenumber for 2D extrapolation in elliptic coordinates reduces to

$$k_{\xi_3}|_{k_{\xi_2}=0} = \pm\sqrt{A^2 s^2\omega^2 - k_{\xi_1}^2 + \mathrm{i}k_{\xi_1}\tan\xi_1 - \frac{1}{4}\tanh^2\xi_3}. \quad \text{(B-12)}$$

LIST OF FIGURES

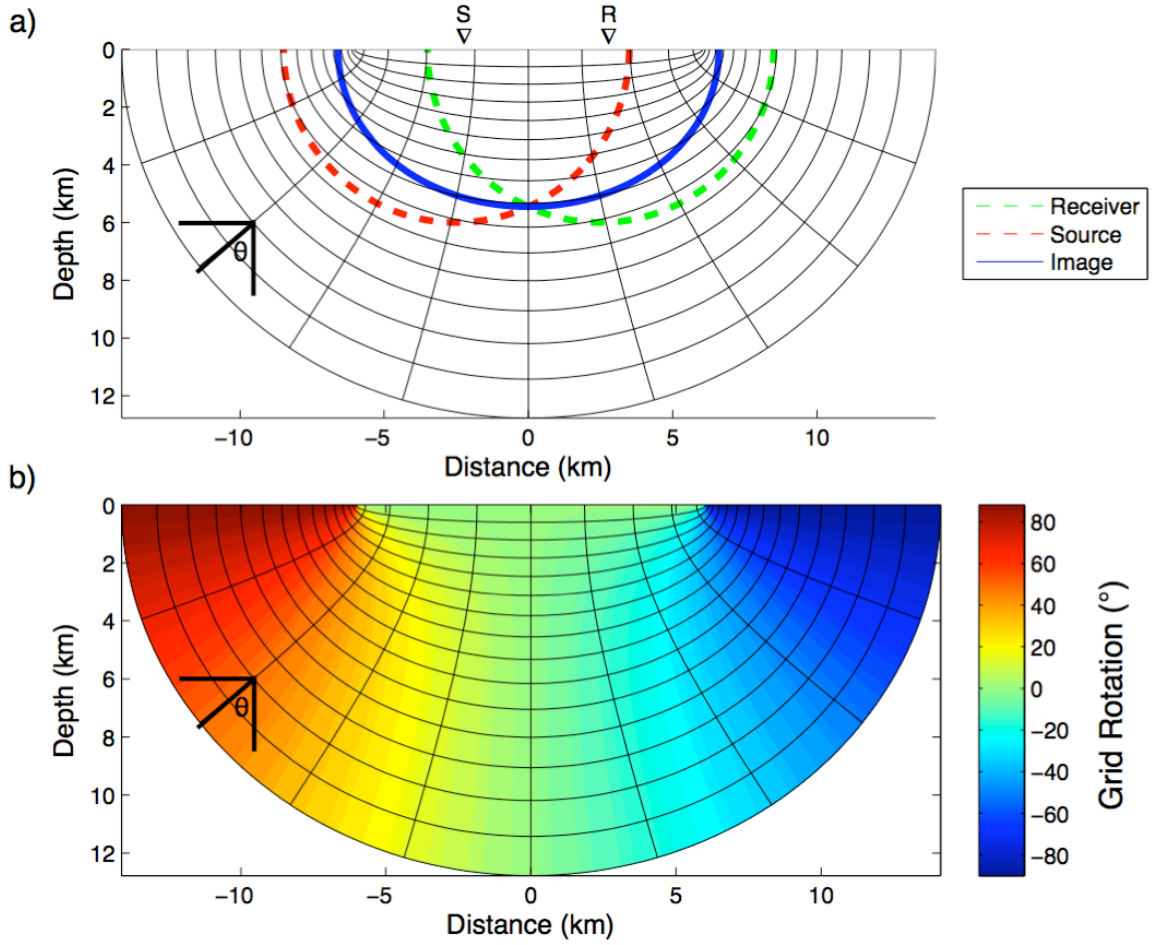

Figure 1: Illustrations of elliptic coordinate system. a) Constant-velocity imaging experiment with punctual source and receiver wavefields (dashed lines) from locations marked S and R, respectively. The corresponding image is an elliptic isochron surface derived by cross-correlating the source and receiver wavefields (solid line). b) Grid rotation angles for the elliptic coordinate system.

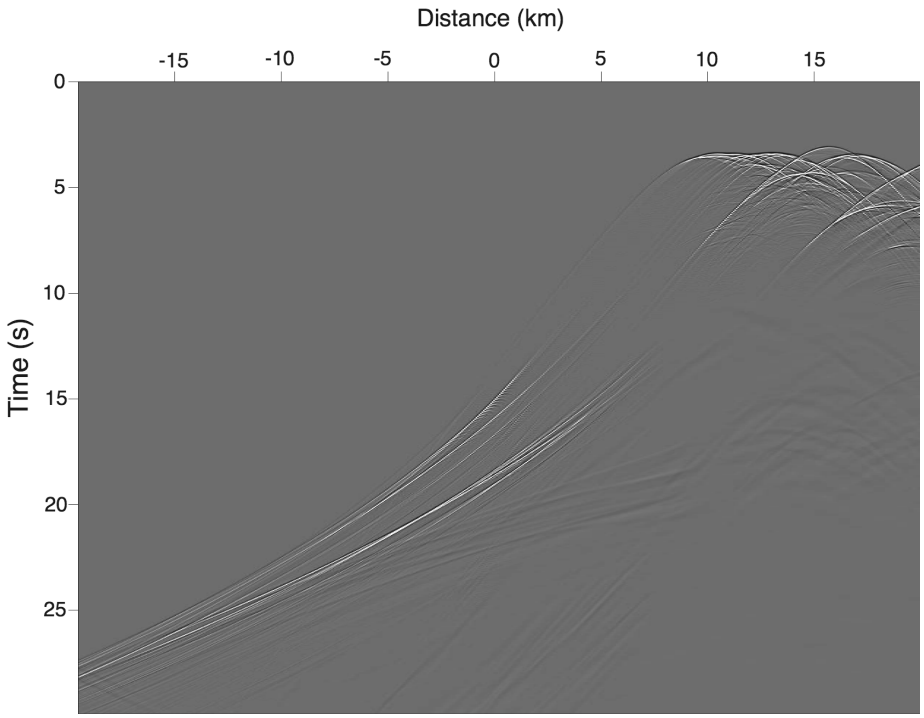

Figure 2: Post-stack turning-wave data. Data set generated by two-way time-domain finite-difference modeling from all salt body edges of the velocity model in Figure 3a.

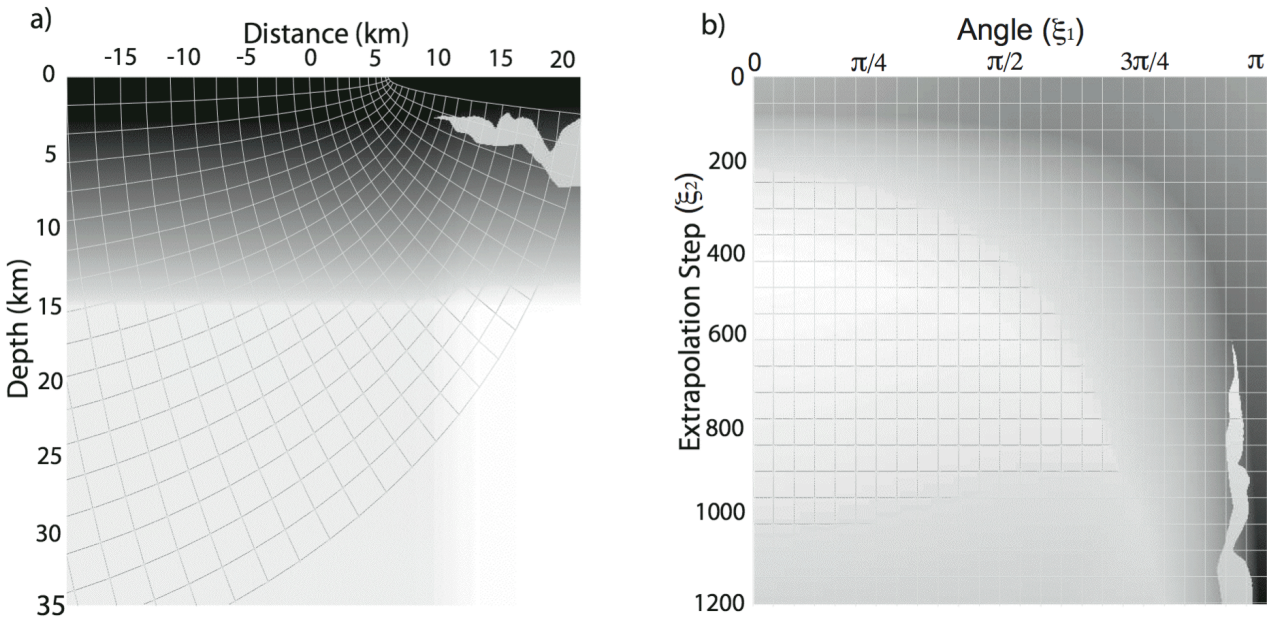

Figure 3: Post-stack turning wave model. a) Velocity model used to generate turning wave data in Figure 2 with coordinate system overlain. b) Effective slowness model s_{eff} in elliptic coordinates.

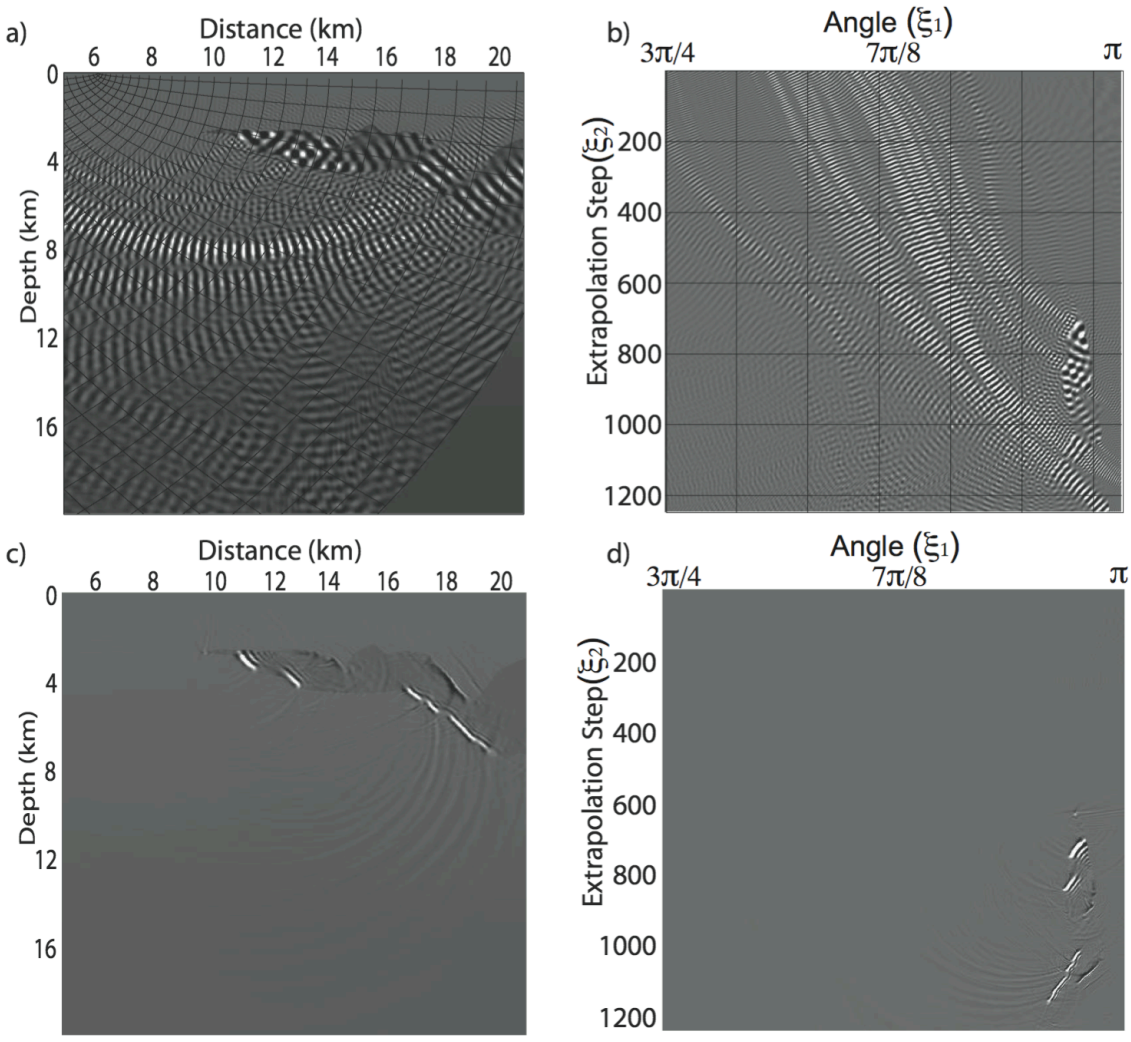

Figure 4: Post-stack turning wave migration result. a) Monochromatic Cartesian image with overlain elliptic coordinates. b) Monochromatic elliptic coordinate image. c) Broadband Cartesian image. d) Broadband elliptic coordinate image.

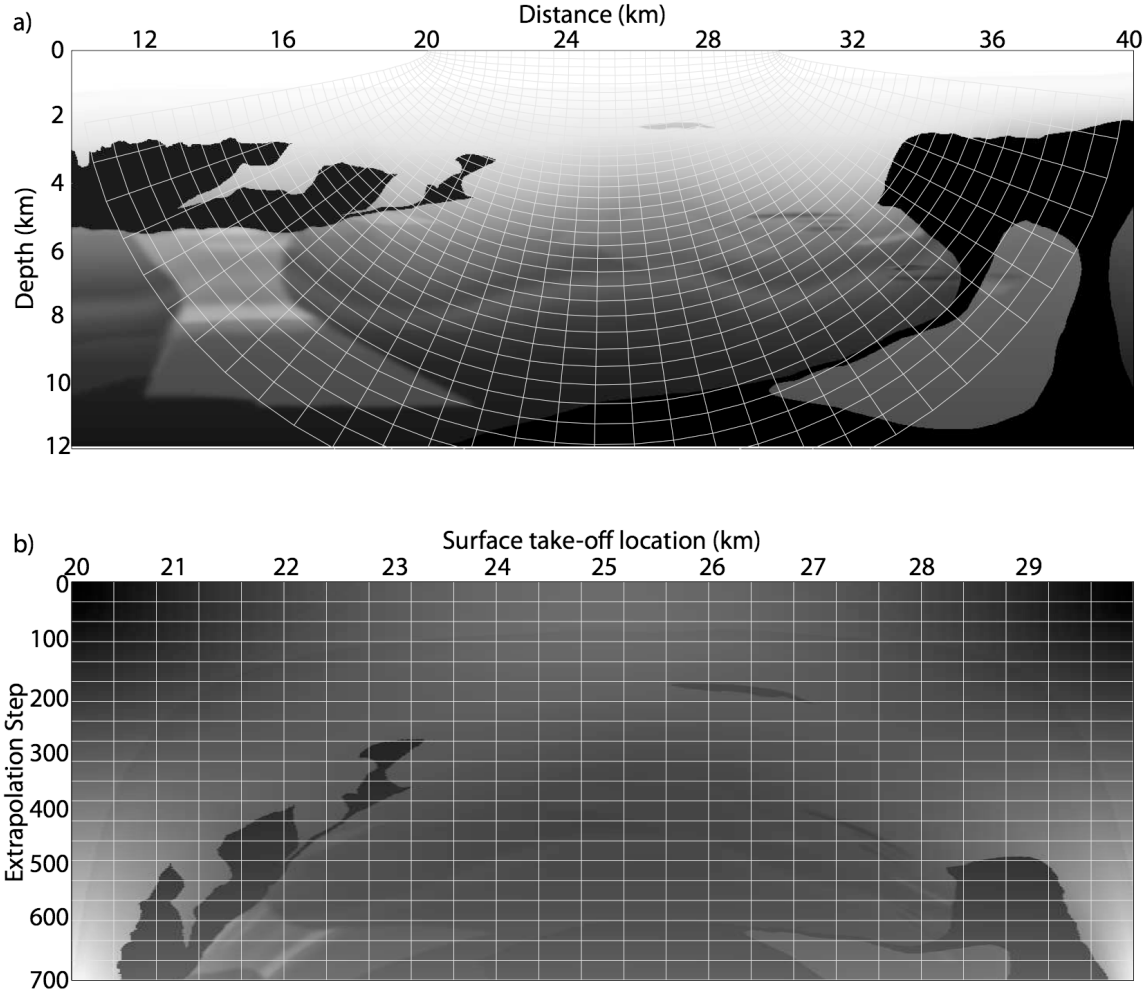

Figure 5: Prestack migration test in elliptic coordinates. a) benchmark synthetic velocity model with the elliptic coordinate system overlain. b) Effective slowness model in the transformed elliptic coordinates system.

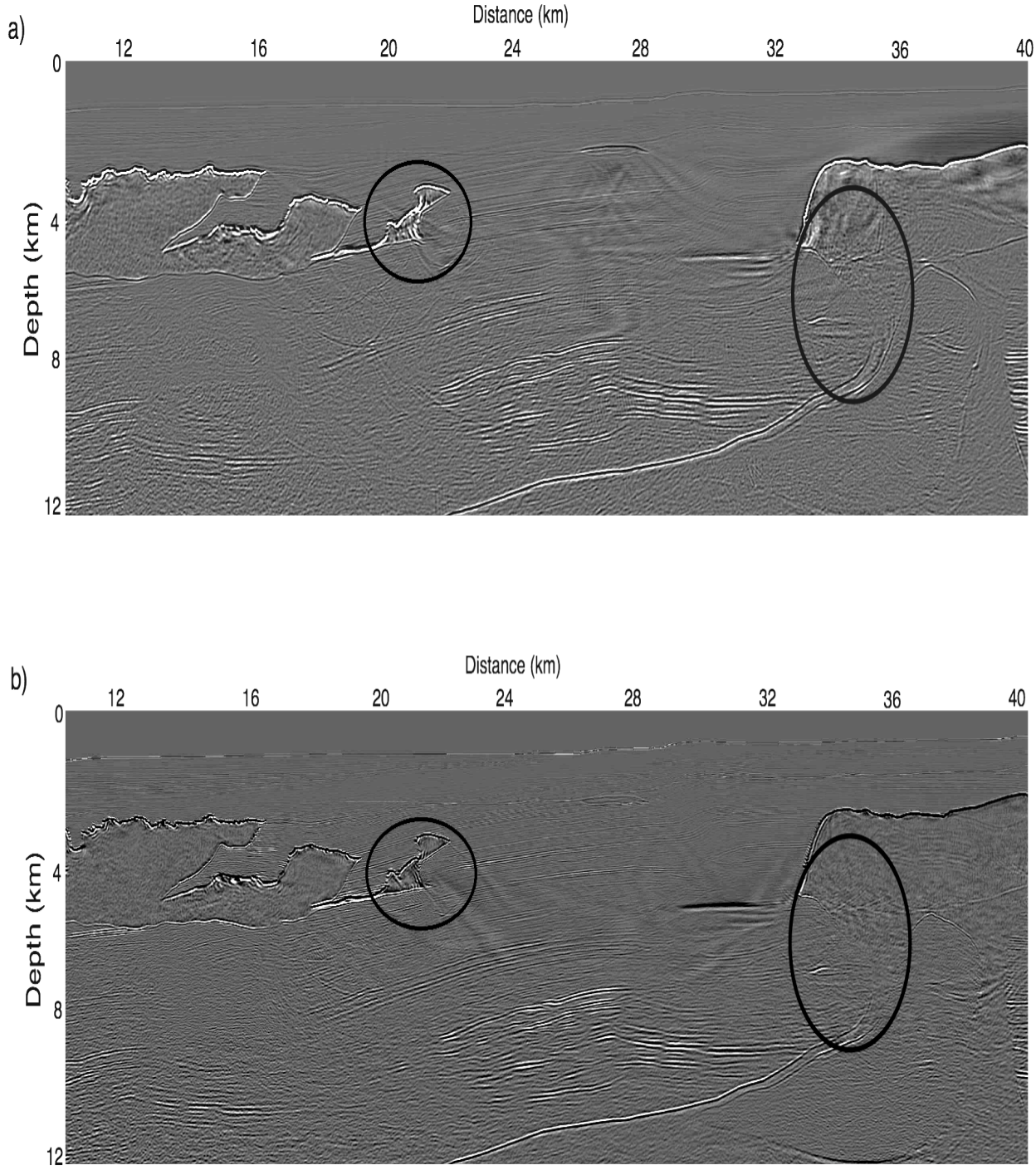

Figure 6: Synthetic migration results. a) Elliptic-coordinate migration result using finite-difference propagators. b) Cartesian migration result generated by finite-difference extrapolators of equivalent accuracy to those in Panel a.

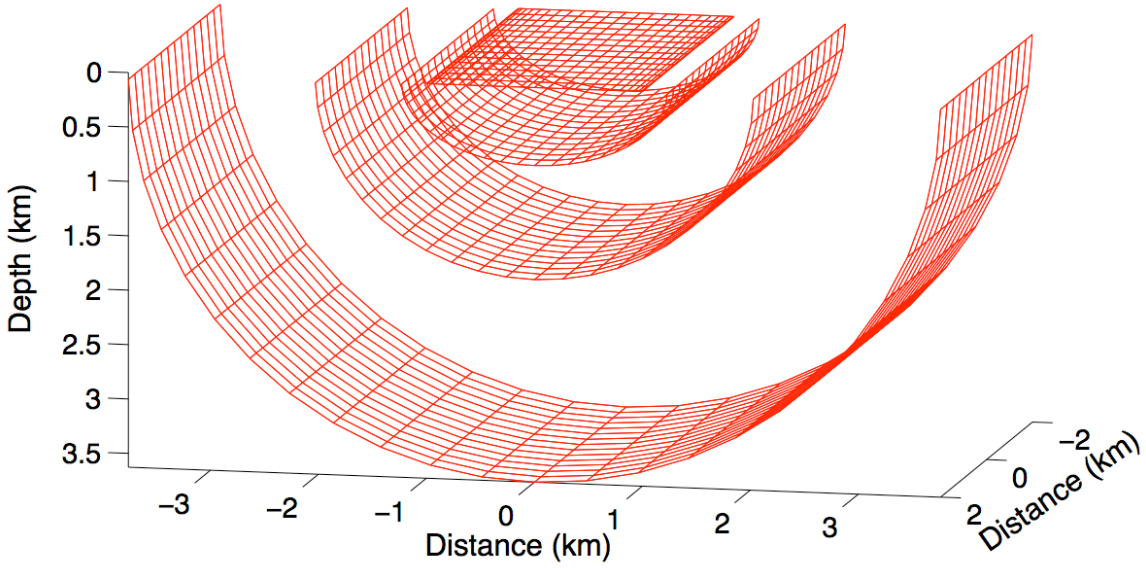

Figure 7: Four extrapolation steps of an elliptic cylindrical coordinate system.

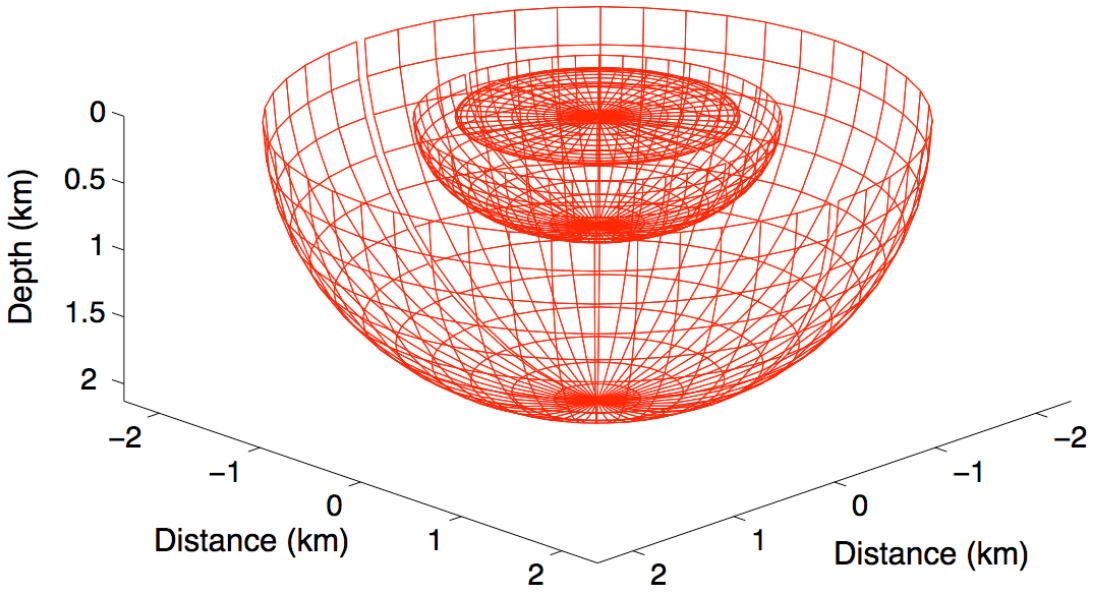

Figure 8: Three extrapolation steps of an oblate spheroidal coordinate system.